

Echo-Planar Imaging: Magnetic Resonance Imaging in a Fraction of a Second

MICHAEL K. STEHLING, ROBERT TURNER, PETER MANSFIELD

Progress has recently been made in implementing magnetic resonance imaging (MRI) techniques that can be used to obtain images in a fraction of a second rather than in minutes. Echo-planar imaging (EPI) uses only one nuclear spin excitation per image and lends itself to a variety of critical medical and scientific applications. Among these are evaluation of cardiac function in real time, mapping of water diffusion and temperature in tissue, mapping of organ blood pool and perfusion, functional imaging of the central nervous system, depiction of blood and cerebrospinal fluid flow dynamics, and movie imaging of the mobile fetus in utero. Through shortened patient examination times, higher patient throughput, and lower cost per MRI examination, EPI may become a powerful tool for early diagnosis of some common and potentially treatable diseases such as ischemic heart disease, stroke, and cancer.

SINCE THE INCEPTION OF MAGNETIC RESONANCE IMAGING (MRI) in 1973 (1), its application in humans has been hampered by the long data acquisition times of several minutes. Thus MR images were prone to motional artifact caused by such physiological motions as heartbeat, blood flow, bowel peristalsis, breathing, or voluntary movements of severely ill or uncooperative patients, such as children (2). As early as 1977, however (3), a technique was devised, echo-planar imaging (EPI), that in principle permitted much faster scan times of 30 to 100 ms. Because of its perceived technical complexity and additional cost, few laboratories worked on the development of this method. Most MRI scanning has been performed with the conventional spin-echo (SE) technique, which is limited by motional artifact mainly to the central nervous system (CNS) and the musculoskeletal system (80 to 90% of all MRI exams). The long examination times (1 to 2 hours) also restrict patient throughput, keep costs per examination high, and exclude some potential patients. In 1985 and 1986 improved "gradient-recalled echo" (GRE) techniques brought acquisition times down to ~15 s (4). Images could be formed in a breathhold, which reduced respiratory artifacts. Improvements in GRE hardware in 1989 brought image acquisition times down to the range of seconds (5), permitting imaging of all organs of the human body including the heart, but unavoidable limitations still exist.

In the meantime, Mansfield's laboratory (6) and Rzedzian and Pykett (7) have developed EPI to clinical maturity and demonstrated

the potential of this technique. Since 1985 there has been a surge of EPI applications, pursued in many laboratories worldwide, and the technique is becoming more widely available. In this article we review technical aspects and the wide range of applications in medicine and research that are possible with real-time MRI.

What Is MRI?

As the name indicates, MRI (8) is derived from nuclear magnetic resonance (NMR) (9), in which magnetic nuclear spins aligned by a large uniform magnetic field are resonantly excited by a radio-frequency (RF) field. The resonant (Larmor) frequency is proportional to magnetic field. In MRI, strong (up to 20 mT m⁻¹) external linear magnetic field gradients are applied across the imaging region. Thus different points in space become identified by different resonance frequencies, which allows the location of nuclear spins emitting RF fields to be determined by their frequency. The signal amplitude at a given frequency gives the spin concentration at that point in space.

Various methods have been devised for mapping tissue with NMR. Early schemes were derived from computed tomography and used filtered back-projection algorithms (10). Present-day MRI is based on the principles of Fourier transform (FT) NMR (11). In two-dimensional (2D) FT MRI (11), the spatial distribution of protons within a sample, $\rho(x,y)$, is mapped by rendering their Larmor precession frequency spatially dependent by magnetic field gradients. After slice-selective RF excitation of a planar slab (12), the detected signal $S(t)$, in the presence of a linear magnetic field gradient G_x applied for a time t_x , is

$$S(t_x) = \int \rho(x,y) \exp \left[i\gamma \int_0^{t_x} G_x(t) x dt \right] dx dy \quad (1)$$

where γ is the gyromagnetic ratio, 42.6 MHz T⁻¹ for protons. A second, perpendicular field gradient G_y , applied consecutively for a time t_y , modifies the signal to

$$S(t_x, t_y) = \int \rho(x,y) \exp \left[i\gamma \int_0^{t_x} G_x(t) x dt + i\gamma \int_0^{t_y} G_y(t) y dt \right] dx dy \quad (2)$$

The Fourier transform of this equation yields $\rho(x,y)$, the MR image. In conventional methods, one gradient (the read gradient) is maintained constant while data are acquired, but in EPI a time-varying read gradient is used (see below). It was pointed out early in the development of MRI (13) that by making the simple substitutions

$$k_x = \gamma \int_0^{t_x} G_x(t) dt \text{ and } k_y = \gamma \int_0^{t_y} G_y(t) dt \quad (3)$$

the MR signal can be expressed in terms of spatial frequencies k . Just as in the diffraction limit in optics, it is $\lambda = 2\pi/k$ that determines the spatial resolution obtainable in MRI, and not the wavelength of the

M. K. Stehling is in the Department of Cardiology, Friedrich Alexander University, and at Siemens AG, 8520 Erlangen, Germany, R. Turner is in the Laboratory of Cardiac Energetics, National Institutes of Health, Bethesda, MD 20892, and P. Mansfield is in the Department of Physics, University of Nottingham, Nottingham, United Kingdom.

RF at the Larmor frequency. The spatial frequency coordinate axes k_x and k_y (typically called the read and phase-encode directions) span k -space, the two-dimensional, inverse Fourier transform of the MR image. Each MR imaging technique, defined by its time sequence of gradients, results in data sampling over a different trajectory in this space. The "diffraction pattern" of the object (Fig. 1A) is characteristically peaked around the k -space origin, and when the time evolution of the gradients carries the sampling trajectory past this point, a sharp maximum in the NMR signal, known as an "echo" (14), is observed. In order to generate such an echo, a gradient must be reversed in sign (GRE), or an additional "refocusing" pulse must be applied (SE) after the initial excitation pulse (14). Matrix size and resolution of an MR image depend on the way k -space is digitally sampled by different imaging regimes (see below).

MRI Strategies

For any MRI technique, the principle for the acquisition of an artifact-free MR image remains the same: Its k -space representation needs to be sampled adequately. The time window during which sampling can be performed is limited by the ephemeral nature of the signal $S(t)$ (the free induction decay or FID), which lasts for 50 to 200 ms after a single RF excitation pulse. Between RF excitations, some time (T_R) must be allowed for spins to return to the direction of the large static magnetic field through the slow process of T_1 relaxation (typical T_1 values range from 500 to 2000 ms, and T_R is of similar magnitude). If smaller RF pulses are used that excite only a fraction of the equilibrium magnetization, T_R can be reduced to a few tens of milliseconds, the echoes being formed by field gradient reversal (GRE), as used in such techniques as FLASH, GRASS, and

FISP (4). These methods reduce the signal to noise (S/N) ratio significantly. Contrast depends mainly on variations of T_1 , unless extremely small flip angles are used, which causes a further loss of signal (15). The GRE techniques with acquisition times of less than 1 s and separate spin preparation modules (see below) have become known as turbo- or snapshot FLASH (5).

MRI and Other Medical Imaging Modalities

Ultrasound (US), conventional x-ray computed tomography (CT), and nuclear isotope scanning each map the spatial distribution of a single parameter: acoustic impedance, electron density, and isotope density, respectively. In contrast, MR images can reflect a multitude of parameters. When MRI was first developed it was hoped that observation of variations in proton density and the relaxation times T_1 and T_2 would provide not only high sensitivity to disease processes but also a high degree of tissue specificity, for example, discriminating tumors from inflammatory processes and normal tissue (16). However, even with accurate MR parameter quantification techniques, this specificity has not been achieved. As a result, there was a shift of emphasis; sensitivity to pathology was increased by improving image resolution and contrast, exploiting the potential of MRI for multiplanar, high-quality anatomical mapping (17). Only recently, advanced NMR techniques for observing variations in metabolite concentration, flow, and perfusion have begun to show promise in the identification of tissue pathology (18). With the introduction of fast and ultrafast imaging regimes such as FLASH, turboFLASH, and a maturing EPI technique there has been a revived interest in functional, rather than merely anatomical, MRI studies, and increasing success in imaging of moving organs such as the heart and the gastrointestinal tract (19).

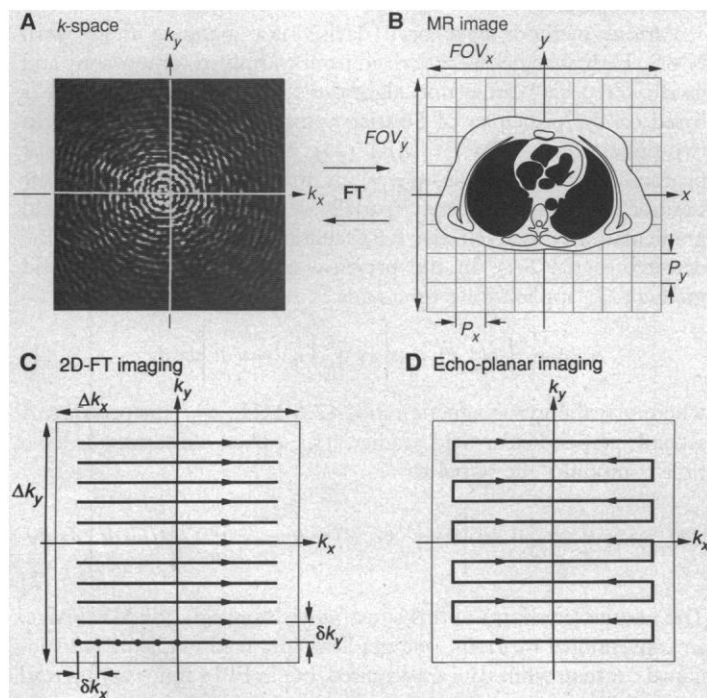


Fig. 1. (A and B) The Fourier transform relation between (A) k -space, which represents the MR raw data, and (B) the MR image. (C) In conventional 2D-FT MR, k -space is sampled in n consecutive acquisitions along lines parallel to the k_x -axis, each line representing a digitally sampled spin or gradient echo. Nominal image resolution, or pixel size P , is determined by the highest spatial frequencies sampled, $P_x = 2\pi/\Delta k_x$ and $P_y = 2\pi/\Delta k_y$. The field of view (FOV) is determined by $FOV_x = 2\pi/\delta k_x$ and $FOV_y = 2\pi/\delta k_y$. (D) In EPI, k -space is sampled in a single, continuous k -space trajectory within a fraction of a second.

EPI Technique

In contrast with conventional MR, where the acquisition of each k -space line requires a fresh spin excitation (Fig. 1C), in EPI a different k -space sampling strategy is used. After a single spin excitation, the whole of k -space is sampled most efficiently in a

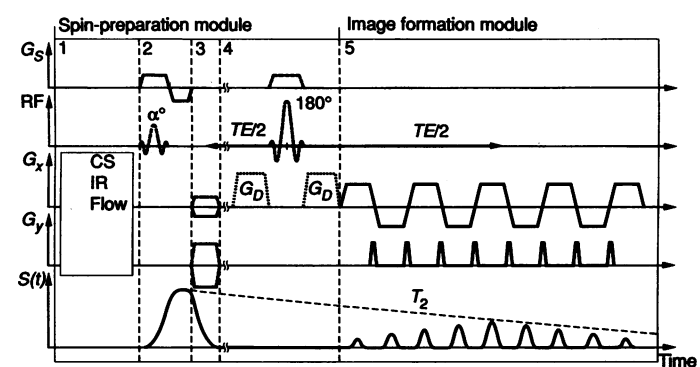


Fig. 2. Diagram of a typical EPI sequence which shows the time dependence of the three orthogonal gradients G_x , G_y , G_z , the radio-frequency pulses RF, and the gradient echo train thus produced, $S(t)$. The choice of axes s , x , and y is made by the operator, which allows any oblique slice to be selected if the imaging system has adequate gradient equipment. Box 1 contains optional pulses for fat or water suppression, CS, T_1 -weighting with inversion recovery, IR, or flow encoding. Box 2 is for selective excitation. Boxes 3 and 4 show the required pulses for gradient-recalled echo (full lines) and spin-echo (broken lines) EPI. The largest echo is formed at a time TE after the initial RF pulse. Optional diffusion sensitization gradients are shown in gray. The dashed line " T_2 " in $S(t)$ indicates the inevitable signal decay during EPI sequences that limits the duration of the acquisition window.

single, continuous trajectory (Fig. 1D) by generating all of the echoes required, up to 256 in a single FID (Fig. 2). Since the decay of $S(t)$ is governed by the transverse relaxation time T_2 ($T_{2,\text{brain}} = 80$ ms and $T_{2,\text{muscle}} = 50$ ms) and field inhomogeneity (in the case of gradient echoes), data acquisition needs to be completed within 50 to 100 ms. When this can be achieved, more complete use is made of the available spin magnetization than with conventional MRI, and the S/N ratio per unit time is consequently much greater (8), although the image is more vulnerable to distortion due to magnetic field inhomogeneity.

The echoes can either be formed as gradient echoes, as in true EPI sequences [MBEST (6, 20), BEST (21), FLEET (22), InstaScan (7), Spiral and Square Spiral EPI (23)] or as spin echoes (RARE) (8, 24). The EPI pulse sequence diagram (Fig. 2) illustrates the typical, rapidly switched, frequency-encoding gradient G_x that generates the gradient echo train $S(t)$. The rise and fall times of the gradient are of the order of 100 μs , rendering the gradient waveforms trapezoidal. The fast rise and fall times of such waveforms require low-inductance coils—100 μH in one system—with low efficiency (0.04 mT $\text{m}^{-1} \text{A}^{-1}$), and thus put severe demands on the gradient drivers, which in that system supply up to 1000 A at 320 V. Alternatively, the waveform may be sinusoidal (7), which requires more complicated data sampling or image processing, but allows the gradient coils to be driven as part of a resonant LC tank circuit, with considerably reduced power requirements. Phase encoding, in which the k -lines are spaced out along k_y (Fig. 1D), is established by pulses or “blips” of the phase-encoding gradient G_y , while the read gradient is being switched. Three-dimensional data acquisition with EPI is possible in various ways (25).

The typical modular structure of EPI sequences is shown in Fig. 2. A spin-preparation module, which can be used to encode a variety of MR parameters such as T_1 , T_2 and flow and incorporates a fat-water separation module, is followed by the EPI image formation, or read-out module (26). The relative independence between spin-preparation and imaging modules in EPI allows fast and interactive optimization of imaging parameters such as contrast without any fundamental changes of the sequence.

Proton density, T_1 , and T_2 are the most important MR parameters for differentiation between the various organs as well as normal and pathological tissue. In diseased tissue both relaxation times are often increased, but they can have opposite effects on image

contrast. In the worst case, this effect can lead to a cancellation such that pathological tissue appears normal (27). A careful separation between T_1 and T_2 contrast effects is thus necessary. This separation has not been easy in fast MRI such as turboFLASH, although good progress has recently been made by incorporation of a spin-preparation module (28). EPI has an inherently modular sequence structure, which allows real-time changes in contrast modality (Fig. 3). Comprehensive mapping of these NMR parameters has been demonstrated (29).

In tissue, two species of protons give rise to the principal NMR signal, those in olefinic hydrocarbon chains of fat and those of free water. Their resonance frequencies differ by 147 Hz T^{-1} because of the different electron densities that surround these protons, an effect known as the chemical shift (CS). In a 100-ms EP image, the bandwidth separation between pixels in the blipped gradient direction is only 10 Hz (total bandwidth 160 kHz, 128 by 128 pixels) and thus a misregistration of 15 pixels per tesla between images of the two species occurs. Selective eradication of the signal of either proton species in the fat-water separation module avoids this artifact and provides pure water or fat images that facilitate organ delineation. All-proton EPI images can be synthesized from two acquisitions.

The Problem of Motion

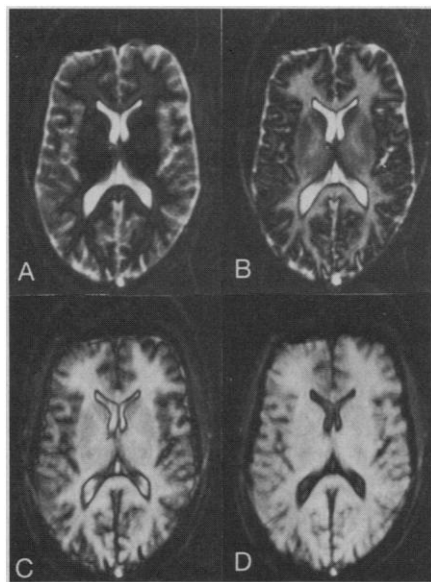
In conventional MRI, persistent image artifacts arise from motion and manifest themselves as blurring, ghosting, and bandlike signal intensity variations that can obscure or even mimic pathology (2). Many schemes have been devised to reduce these artifacts, from the use of restraining straps to sophisticated gating and gradient-motion compensation methods (30). Few are routinely used since most do not resolve the problem and prolong the examination time intolerably. Conceptually, motion-related problems can be obviated most easily by reducing the imaging time sufficiently that the object appears static. The maximum velocities of organs encountered in the human body, except for blood flow in arteries or at sites of stenosis (up to 1 to 10 m s^{-1}), do not exceed 10 cm s^{-1} (heart), and acquisition times of 50 to 100 ms “freeze” such motion in an instantaneous “snapshot” exposure.

Applications of EPI

Cardiovascular system. Conventional MR images of the heart are composites from cardiac phase-synchronized (gated) fractional acquisitions over as many as 256 heart cycles (31). Arrhythmias and irregular breathing, which are more frequent and pronounced in the ill, often make it impossible to obtain diagnostic information during the limited time the patient can endure to lie in the imager. EPI can provide multiplanar static and movie-loop images of the heart in real time. These images allow the assessment of cardiac morphology and function, such as contractility and blood flow dynamics, even in severely ill or uncooperative patients such as infants. For dynamic studies, up to 20 images can be obtained per heart beat. For comparison, state-of-the-art CT (Imatron) can give 20, US 30, and cardiac angiography 90 frames per second (32). However, real-time MRI has several advantages. It is free from ionizing radiation, allows several tissue parameters to be probed, and affords free choice of image-plane orientation, which is of great importance for the heart, whose main axes lie obliquely in the thorax. The MRI method provides a tool for simultaneous morphologic and functional studies.

Of utmost importance in cardiology is the assessment of myocardial perfusion with blood; 30% of deaths between the ages of 35

Fig. 3. Interactive control of T_1 contrast in brain imaging. Shown are four transaxial EPI brain images (A, B, C, and D) of a single slice acquired with a preparation module that inverts the nuclear spins prior to the rest of the sequence at four different times, which increase up to 2 s. The change in contrast is easily apparent and reflects the variations in T_1 within brain tissue; FOV, 20 cm; slice thickness, 5 mm; 100-ms acquisition time per image; and pixel matrix 128 by 128. [Courtesy of F. Schmitt and M. K. Stehling, Siemens Medical Engineering Group, Siemens AG, Erlangen, Germany]



and 64 in the United States are caused by myocardial infarction, often without prior symptoms. The time course of the distribution of an NMR tracer substance (contrast agent) in the myocardium under physical exercise or pharmacological stress may be observed by using EPI (33), and thus myocardial areas at risk for infarction can be delineated. This approach could allow appropriate therapeutic measures, such as coronary angioplasty, to be taken. After restoration of blood flow, follow-up coronary angiography could be replaced by noninvasive EPI studies. The drawback of other real-time MR techniques is their inability to provide information about the whole myocardium in the time typically available for imaging (33).

Flow imaging. Although EPI freezes all anatomic motion, it displays an exquisite sensitivity to flow because the relatively long acquisition times can lead to large velocity-induced variations in the phase of the signal. The evolution of turbulence in fluid can thus be observed with accuracy and ease. Slow and laminar fluid flow can also be observed in detail by EPI, either through the effect of unsaturated spins entering the imaging plane (inflow effect) or with flow encoding (34–36). EPI has been used to study turbulent flow in valvular heart disease, where jets originating from stenosed or leaky valves can be observed [see Fig. 4 (37)]. Laminar and turbulent cerebrospinal fluid (CSF) flow has been depicted by EPI in cases of hydrocephalus (35), an imbalance between the production and drainage of the fluid that partially fills and also supports the brain. Flow patterns can be indicative of the different causes and a guide to the treatment of this disease, which often manifests itself in children (38). Others (39) have studied structured fluid flow in vortex rings in water and have shown that EPI is able to provide a precise fingerprint of complex fluid dynamics. Precise flow-velocity mapping in the arteries supplying the brain has been reported (36), as has some success with flow quantification in coronary arteries, which are most difficult to depict because of their small size, tortuosity, and mobility.

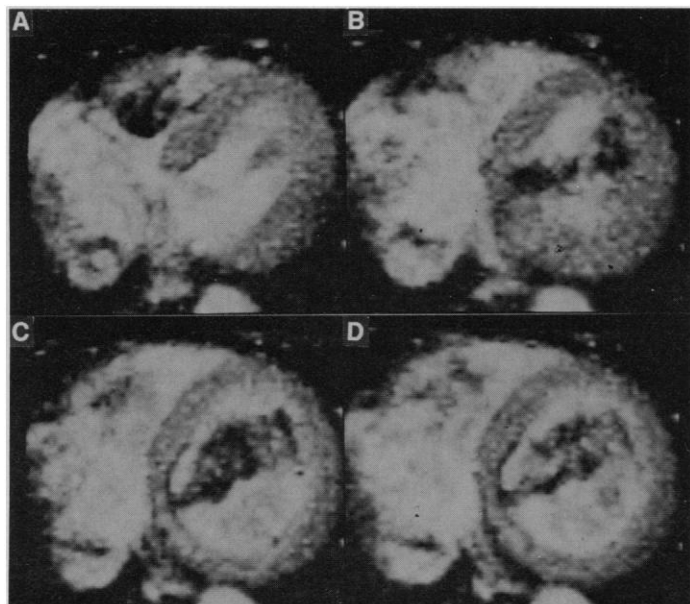
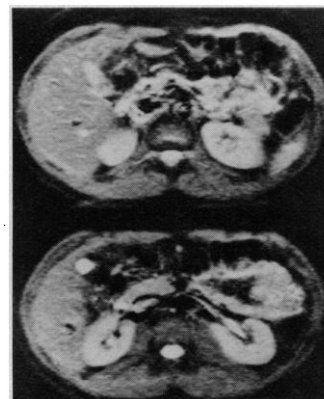


Fig. 4. Echo-planar images of the human heart acquired in 0.1 s on a low-field scanner developed at the University of Nottingham. The images show ventricular function and blood flow dynamics. Myocardial hypertrophy is evident at maximal contraction in systole (A) and is due to volume overload resulting from regurgitation of blood through an incompetent aortic valve throughout diastole [early (B), mid (C), and late diastole (D)]. [Courtesy of M. K. Stehling and P. Mansfield, Department of Physics, University of Nottingham, Nottingham, United Kingdom]

Fig. 5. Single-shot abdominal echo-planar images, pixel matrix 128 by 128, at the level of the kidneys. A high level of detail, with no motional blurring or ghosting, can be seen in the liver and kidneys. $FOV = 40$ cm; total acquisition time, 64 ms; slice thickness, 10 mm. The two slices shown are spaced 15 mm apart. [Courtesy of B. R. Rosen, Massachusetts General Hospital, Boston, Massachusetts 02114]



Abdomen. The liver is clinically of great interest. Metastases from 45% of all malignant tumors become trapped in its filterlike sinusoids and can be successfully treated by resection or local chemotherapy if detected early (40). The imaging modality must detect small focal liver lesions with high sensitivity and differentiate them with high specificity from a range of benign lesions, of which simple liver cysts and hemangiomas (10% of the population) are the most common. Theoretically, MR is the modality of choice, since it combines high spatial resolution with unrivaled multiparametric tissue contrast and can thus provide a high degree of tissue characterization (41). However, the liver undergoes respiratory displacement of up to 13 cm, and movements of the anterior abdominal wall also cause regular motional artifacts. TurboFLASH techniques have yet to provide good T_2 -weighted subsecond images of the liver (27); the resolution and S/N ratio are inadequate for the detection of lesions smaller than 1 cm and are surpassed by EPI (Fig. 5). Furthermore, dynamic contrast agent studies are most sensitive to pathology during the first 2 min after their infusion (41). Multislice EPI techniques allow the whole of the liver to be scanned in 20 levels at repetition rates of 4 to 5 s (42, 43) and may provide inflow profiles of excellent time and spatial resolution, which would aid in the differentiation between hemangiomas and metastases. EPI abdominal imaging has also been used to quantify peristaltic activity (44).

Brain imaging. It might be thought that the EPI technique would have least value in that most static of organs, the brain, but even here motion artifact can compromise conventional MRI. In terms of resolution alone, recent single-shot EPI brain images with pixels as small as 1.5 mm by 1.0 mm by 5 mm compare well with conventional SE images. If higher resolution is required (Fig. 6), data from a small number of successive acquisitions can be pieced together to cover k -space in several segments (45), since the total number of echoes obtainable per excitation has an upper limit, perhaps 256. The total acquisition time for a 512 by 256 matrix may be kept shorter than 400 ms, the concomitant drop in S/N ratio being regained with closely fitting, high-quality head RF coils. The net scan time for a high-resolution 40-plane brain study can be as little as 20 s. EPI of the brain has already made a notable impact in three areas: (i) molecular diffusion, (ii) mapping of changes in temperature, and (iii) cerebral perfusion.

Molecular diffusion is of great interest because it can provide microstructural information. However, even on a time scale of seconds, conventional MRI methods combine diffusion effects with the continual small involuntary bulk motions of brain tissue (46). During a typical image acquisition time of about 2 min information regarding diffusion is often irrevocably scrambled. In order to observe the effects of diffusion in an MR image (47) a pair of large magnetic field gradients must be applied (Fig. 2) after the nuclear

spins have been excited (48) but before data acquisition. The image becomes extremely sensitive to motion of any kind. In the absence of artifacts, an image obtained after application of "diffusion gradients" (as they are termed) is least intense where diffusion is most rapid. Where bulk motion is present, however, conventional diffusion-weighted images (48) show extensive "ghosting" in the phase-encoding direction that prevents quantification of the diffusion constant. This effect very often occurs in studies of the human brain (49), although in paralyzed animals good diffusion maps of the brain have been obtained (50).

With little possibility of bulk motion artifact, EPI has been used very successfully (51) to obtain reliable measurements of the diffusion constant D in human brain. Depending on tissue type and orientation, D varies between one-tenth and one-third of that of pure water at body temperature. A special small-scale gradient coil has been used, which encloses only the head, to obtain rapid enough switching and large enough gradients so that a conventional MR scanner can obtain EP images. A typical diffusion map is shown in Fig. 7. Because D has recently been shown to change dramatically within minutes of an ischemic insult (52), evaluation of stroke at a very early stage in human victims, before irreversible neuronal damage, may be possible.

The direction of the magnetic field gradients determines the direction in which diffusion is measured. Observations of cat (53) and human brain (49, 51) show that in myelinated white matter tracts, diffusion is highly anisotropic, with D being two to three times greater along the nerve fiber direction than transverse to it. This observation is still not fully understood.

Diffusion imaging can also be used to map temperature in deep-lying tissue. The sensitive temperature dependence of D for

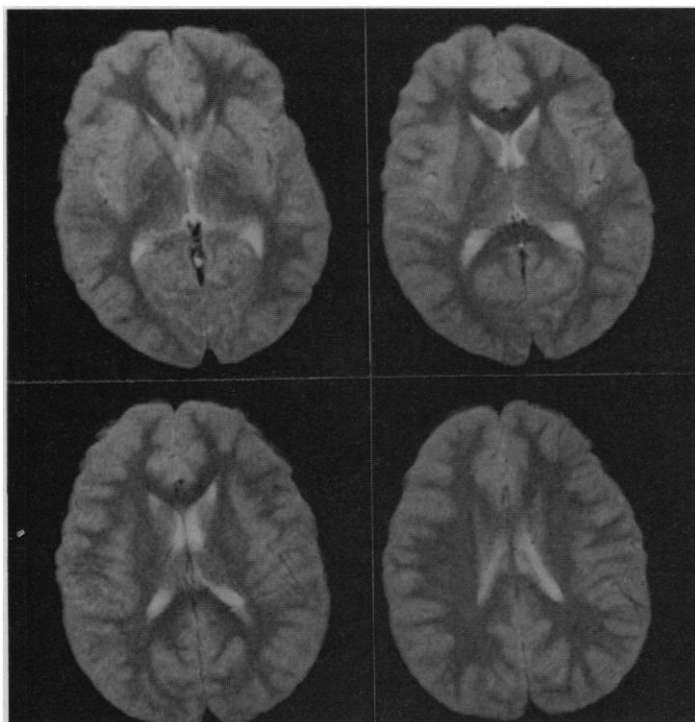


Fig. 6. Four high-resolution two-pass EPI axial images of the brain of a volunteer at different levels spaced 7 mm apart. This resolution was obtained by dividing the sampling of data in k -space between two RF shots that were spaced 6 s apart. This procedure lessens the demands on imaging hardware but increases the risk of distributed motional artifact (not visible here). In-plane resolution, 1.5 mm by 0.8 mm; slice thickness, 5 mm; 128 by 512 pixel matrix; total acquisition time 2×64 ms per image; total scanning time, 12 s. [Courtesy of M. S. Cohen, Massachusetts General Hospital, Boston, Massachusetts 02114]

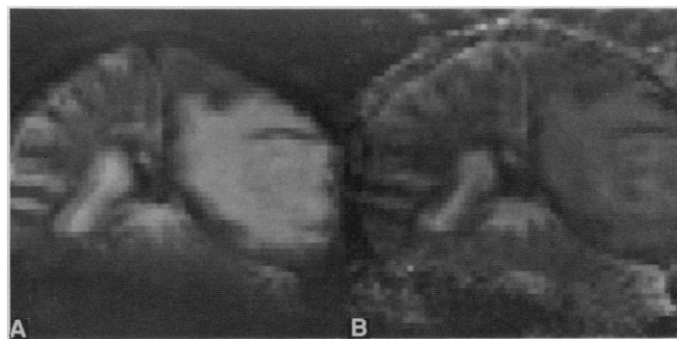


Fig. 7. Mapping of diffusion coefficient of water in human brain. (A) A T_2 -weighted 64 by 64 EPI coronal image with spatial resolution of 2.5 mm by 2.5 mm by 10 mm, echo time, 100 ms, acquisition time per image 50 ms, obtained with a GE Signa 1.5-T MRI scanner with a laboratory-built gradient head coil. The subject was a patient suffering from a large malignant glioma surrounded by edema. (B) The diffusion-coefficient image computed from 16 EPI images with progressively larger diffusion gradients applied before data acquisition. A nonlinear least-squares fit algorithm was used to extract the diffusion coefficient D for each voxel from the dependence of signal intensity on gradient; the image intensity is proportional to D . The enhanced brightness in the neoplastic region of the first image (A), corresponding to an increased relaxation time T_2 , is less apparent in the diffusion image (B), showing that the lesion is not fluidlike, since its diffusion coefficient is much lower than that of the cerebrospinal fluid in the ventricle of the contralateral hemisphere. [Courtesy of D. Le Bihan and R. Turner, National Institutes of Health, Bethesda, Maryland 20892]

water, $\sim 2\%$ change per degree Celsius, allows changes in internal temperature to be observed as changes in the diffusion constant map with an accuracy of better than 0.5°C (54). Thus hyperthermia used to destroy cancerous tissue can be monitored. Either laser surgery (55) or RF induction heating (56) may be used, but the crucial problem is to determine exactly when the tissue damage is extensive enough, including all of the diseased tissue and none of the healthy tissue. Surgical implantation of thermocouples is often completely impractical. EPI, with diffusion gradients applied, is capable of providing this information noninvasively and in real time (Fig. 8). This is one instance of interventional radiology, that is, the use of therapeutic techniques under radiological control.

The third area of brain imaging to benefit from EPI is the measurement of cerebral blood flow, or perfusion. Blood takes only a few seconds to pass through the brain. It occupies only 1 to 2% of the tissue volume, but if an intravascular paramagnetic contrast agent is used, the NMR signal from surrounding tissue is greatly affected because of the high magnetic field gradients that are established around the blood vessels. Chelates of rare-earth elements such as gadolinium and dysprosium are widely used to enhance the contrast of tumors and other lesions in conventional MRI because they cross the blood-brain barrier only where it is disrupted by tissue pathology. With the use of EPI it is now possible to follow the initial contrast changes in normal tissue while an injected bolus of intravascular contrast agent makes its first and second passage around the bloodstream (57). Approximate blood volume maps may be inferred. If the arterial input function is measured, the mean transit time of blood through the capillary bed, and hence perfusion itself (58), may also be obtained.

Recent work (Fig. 9) has demonstrated regional changes in blood volume measured by this technique when volunteers were subjected to visual stimulation (57). These dramatic results are analogous to those obtained by positron emission tomography (PET) but differ in three important respects. First, with PET the S/N ratio has often been so poor that in order to obtain significant changes in the image related to brain stimulation the results from several subjects were pooled. Only one subject is needed with MR blood flow imaging.

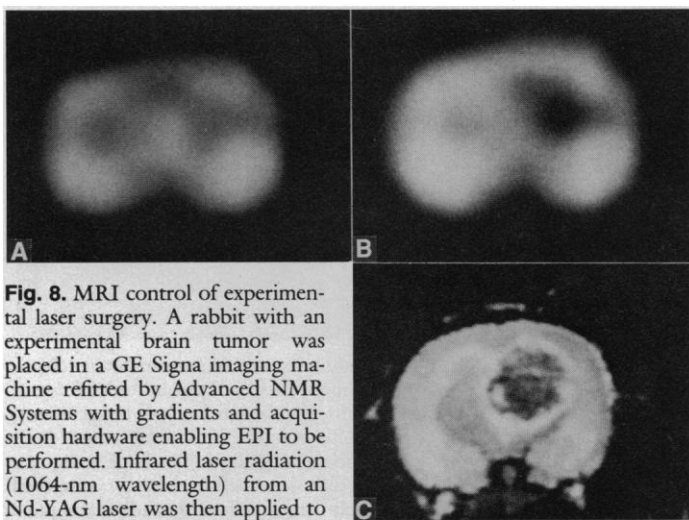


Fig. 8. MRI control of experimental laser surgery. A rabbit with an experimental brain tumor was placed in a GE Signa imaging machine refitted by Advanced NMR Systems with gradients and acquisition hardware enabling EPI to be performed. Infrared laser radiation (1064-nm wavelength) from an Nd-YAG laser was then applied to the tumor by means of a 600- μm fiber optic, while at the same time diffusion-weighted EPI images were obtained, to monitor the temperature rise in the regions affected. (A) and (B) show EPI images before and during irradiation (resolution of 3 mm by 3 mm by 10 mm). The darkened region in (B) manifests the increase in diffusion coefficient caused by the temperature increase. (C) A conventional T_2 -weighted SE image obtained 24 hours after surgery shows the extent of the permanent tissue damage, which corresponds well with the darkened area on (B). [Courtesy of F. A. Jolesz, Department of Radiology, Brigham and Women's Hospital and Harvard Medical School, Boston, Massachusetts 02115]

Second, the spatial resolution of EPI is better, with a typical voxel size of 1.5 mm by 1.5 mm by 5 mm, as compared with 5 mm by 5 mm by 5 mm, achievable with state-of-the-art PET scanners. Third, the contrast agent used in EPI blood flow studies is inexpensive, widely available, and of low toxicity. Similar time course studies have been used to study the severity and extent of experimental ischemia in laboratory animals (59). The technique has also been used to assess cerebral perfusion in patients with brain tumors and stroke (60).

Fetal imaging. The utility of EPI for imaging of the human fetus in utero has been demonstrated (61). A healthy fetus is mobile in the amniotic cavity for most of its intrauterine life, so ultrafast image acquisition is needed to avoid motional blurring and loss of anatomical detail. Among the advantages of MRI over US, the established imaging modality in pregnancy, are the superior contrast provided by MRI, the free choice of imaging planes, which is not limited by available "windows" necessary for the US probe to look through the abdominal wall of the mother, and the three-dimensional capability of MR, which allows exact measurement of fetal organ volumes and hence development. Fetal malformation such as gastroschisis and diaphragmatic hernias has been depicted by EPI (61), and accurate postnatal prognoses have been made. In real-time mode, depiction of the rapidly beating fetal heart (180 beats per minute) has proved feasible (61) (Fig. 10). Imaging of infants without sedation has also been demonstrated (62).

Safety

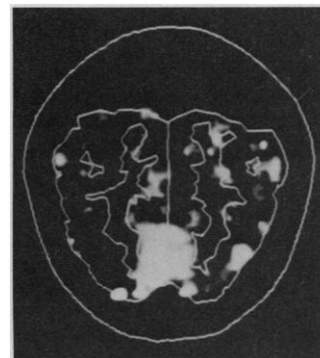
Static and time-dependent (gradient) fields as well as RF irradiation are potential hazards of MRI. Within established Food and Drug Administration recommendations, no ill effects have been observed in those hundreds of thousands of patients who have undergone MRI to date. By far the most dangerous effect is injury to the patient by metallic objects, which become missiles in the

scanner's strong magnetic fringe field. However, EPI differs from conventional MRI in that very large magnetic gradient fields need to be switched back and forth very rapidly, resulting in peak rates of change of 50 to 100 T s^{-1} , particularly when high resolution at ultrashort acquisition times is desired. Recent investigations have consistently reported sensations ranging from "tickling" to "pain" induced in volunteers exposed to field changes exceeding 60 T s^{-1} (63). This observation has caused some concern, since ventricular fibrillation may result from myocardial current densities of 4 A m^{-2} , induced at 250 T s^{-1} (64). These findings might limit the maximum dB/dt to values below 80 T s^{-1} , and, with maximum image acquisition times of about 100 ms, restrict the obtainable resolution in EPI. However, recent theoretical and experimental results (65) indicate that for all gradient waveforms and at sufficiently high frequencies the critical factor in determining the neural stimulation threshold is not dB/dt , nor $\tau dB/dt$, where τ is the gradient rise-time, but simply the maximum change in B itself. Others have reported similar findings (66). These results suggest that 256 by 256 EPI images with 40-cm FOV could be obtained in less than 100 ms without causing neural stimulation.

Availability

Although the foundations of EPI were laid almost 15 years ago and the first EP images of biological objects and infant patients were generated at the University of Nottingham as early as 1980 and 1983, respectively, EPI has only just become available in a commercial form. The demands EPI puts on scanner hardware components such as the magnet (extremely good field homogeneity), gradient coils (strong gradient fields and low inductance for fast switching), electronics (large bandwidths and high digitization rates) and computers (ultrafast image reconstruction and display and large data memories) have slowed commercialization. Several major suppliers of MR systems are now developing EPI capability on their top-of-the-range scanners that are based on laboratory-built systems (7, 22, 67, 68). The major technical problem in accommodating EPI on commercial systems is producing the very large (10 to 40 mT m^{-1}), rapidly switched (500 to 2000 Hz) magnetic gradient fields without inducing eddy currents in the magnet's metallic structure. A small gradient coil set designed for the head or an extremity is one solution which, like resonant gradient coils mentioned earlier, can

Fig. 9. Functional NMR mapping of the human visual cortex. Light-proof, stimulating goggles were placed over a subject's eyes. Two 4-s intravenous doses (0.1 mmol kg^{-1}) of the paramagnetic contrast agent Gd(DTPA) were administered at half-hour intervals. Spin-echo EPI images were collected at 1-s intervals for 1 min at each administration and spanned the transit of contrast agent through the brain. A surface coil placed over the occipital pole was used to receive the NMR signal, giving a S/N ratio of 170:1 for an oblique slice positioned through the calcarine fissure. The image shows the difference between blood volume maps calculated from the EPI time course images with and without visual stimulation. The solid line is an overlay indicating the boundaries of white matter in this region of the brain. The bright area, which shows an increase of blood volume of 10 to 15%, corresponds in detail with the primary visual cortex. [Courtesy of J. W. Belliveau and B. R. Rosen, Massachusetts General Hospital and Harvard Medical School, Boston, Massachusetts 02114]



also benefit other advanced MR techniques. Low-inductance gradient coil designs require a small number of turns that must be strategically placed to ensure good gradient linearity (69). In addition, the increase in effective inductance resulting from electromagnetic coupling with surrounding conducting structures can be avoided by means of self-shielded coil designs that have an outer layer of windings that cancel out the fringe fields (70). Active shielding or eddy current compensation, or both, which are already used by one manufacturer for routine MR, are likely to be a feature of all future MR scanners, since almost any application would benefit, including MR flow quantification and angiography. A more widespread availability of EPI in clinical institutions can be expected within the next 3 to 5 years.

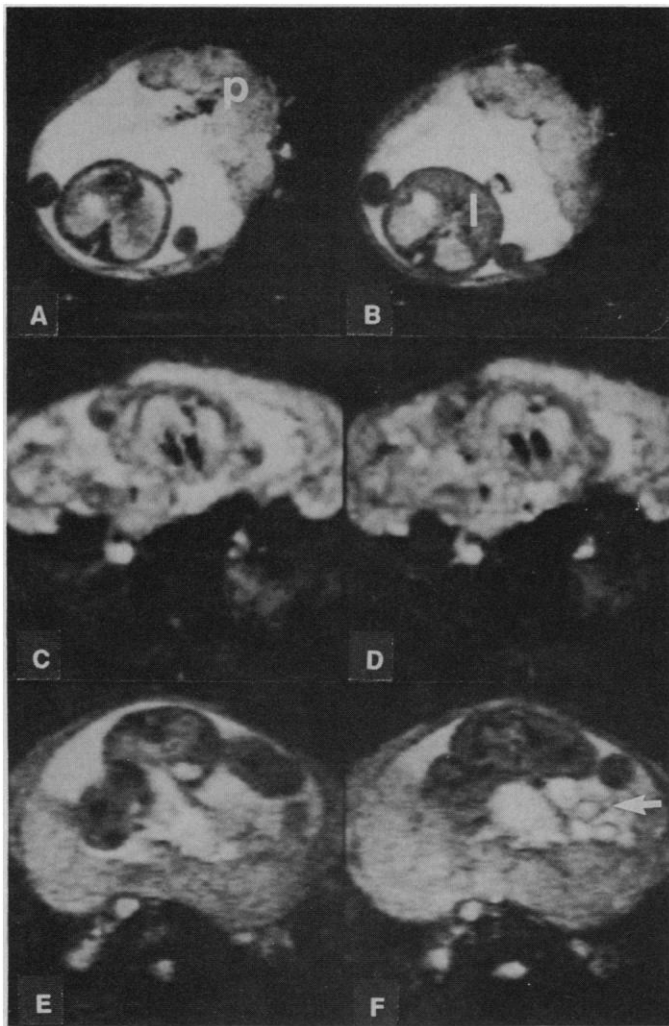


Fig. 10. Single-shot EP images of human fetuses in utero obtained at low field, 0.52 T. (A and B) In cross sections through the fetal abdomen, fetal organs such as liver (l), kidneys, and stomach as well as the umbilical cord and its insertion into the placenta (p) are demonstrated with great clarity and high tissue contrast. Amniotic fluid shows white. Gestational age was 32 weeks. Acquisition time was 128 ms and matrix size 128 by 128 pixels, in-plane resolution 3 mm by 3 mm. (C and D) Thoracic cross sections show left and right chambers of a fetal heart at 26 weeks of gestation at different phases of the cardiac cycle. In utero, the uninflated lungs are filled with alveolar and amniotic fluid and appear bright. Acquisition time: 64 ms. With real-time imaging, movie loops of the fetal heart can be obtained within a single fetal heart cycle. (E and F) A breach in the abdominal wall of a fetus at 36 weeks gestation (E), and the protrusion of the intestines (arrow) into the amniotic cavity (F), were diagnostic of a gastroschisis. [Courtesy of M. K. Stehling and P. Mansfield, Department of Physics, University of Nottingham, Nottingham, United Kingdom]

Impact

In EPI images can be obtained up to 10,000 times faster than in conventional SE MRI, and five times faster than turbo-FLASH. Since images can be obtained and displayed almost immediately in much less than 1 s, a physician operating the EPI scanner can see any part of the human body in real time, as with US. Targeting of pathology is thus facilitated and superfluous images can be avoided. Moreover, by adjusting pulse-sequence parameters in real time during the scanning procedure, lesion-tissue contrast and thus lesion conspicuity can be optimized under visual control. Thus, a range of T_1 or T_2 contrast, or fields of view, can be assessed very rapidly. In contrast, conventional MRI requires the operator to choose imaging parameters "blindly" based on the kind of pathology expected and parameter recommendations that have been compiled in previous clinical studies. This approach may result in suboptimal contrast or complete failure to depict the lesion, even after hours of scanning.

Discussion

EPI is rapidly developing into a mature MRI technique whose speed and image quality have exceeded many expectations. During the last 5 years it has been demonstrated that EPI could greatly enhance the usefulness of MRI by dramatically improving the speed of MRI examinations and by providing functional information hitherto unobtainable with MRI, in addition to high-resolution morphological information. Interest in EPI technology is rapidly growing within many internationally renowned research and clinical institutions. The major capabilities of EPI include:

- 1) Instantaneous image acquisition that excludes motion artifact.
- 2) Image quality resembling conventional, high-quality SE images with resolution in the submillimeter range.
- 3) Most efficient use of the available MR signal available per unit time.
- 4) Unrestricted choice of image contrast, such as proton density, T_1 , and T_2 .
- 5) Modular structure, facilitating simultaneous functional and morphological imaging and interactive operation with real-time control.
- 6) Three-dimensional data acquisition and high temporal resolution for time-course studies.
- 7) Reduced examination times with potential higher patient throughput and lower cost per examination, making MRI available to a larger number of patients and the application of MRI as a screening technique commercially feasible.

The applications described here are only among the first in the development of "snapshot" MRI that may leave the age of "daguerrotype" MRI behind.

REFERENCES AND NOTES

1. P. Mansfield and P. K. Grannell, *J. Phys. C* 6, L422 (1973); P. C. Lauterbur, *Nature* 242, 190 (1973).
2. M. L. Wood and R. M. Henkelman, *Med. Phys.* 12, 143 (1985); R. M. Henkelman and M. J. Bronskill, *Rev. Magn. Reson. Med.* 2, 1 (1987).
3. P. Mansfield, *J. Phys. C* 10, L55 (1977).
4. A. Haase et al., *J. Magn. Reson.* 67, 258 (1986); E. M. Haacke and J. A. Tkach, *Am. J. Roentgenol.* 155, 951 (1990); J. S. Waugh, *J. Mol. Spectrosc.* 35, 298 (1970).
5. D. J. Atkinson and R. R. Edelman, paper presented at the Seventh Annual Meeting of the Society of Magnetic Resonance in Medicine, San Francisco, 20 to 26 August 1988 (book of abstracts, p. 137); A. Haase, *Magn. Reson. Med.* 13, 77 (1990).
6. A. M. Howseman et al., *Br. J. Radiol.* 61, 822 (1988); M. K. Stehling et al., *Radiology* 170, 257 (1989).
7. R. Rzedzian and I. L. Pykett, *Am. J. Roentgenol.* 149, 245 (1987).
8. P. Mansfield and P. G. Morris, *NMR Imaging in Biomedicine* (Academic Press, New York, 1982).

9. F. Bloch, W. W. Hansen, M. Packard, *Phys. Rev.* **69**, 127 (1946); E. M. Purcell, H. C. Torrey, R. V. Pound, *ibid.*, p. 37.
10. J. Radon, *Ber. Math.-Phys. Kl. Saechs. Ges. Wiss.* **59**, 262 (1917); A. M. Cormack, *J. Appl. Phys.* **34**, 2722 (1963).
11. A. Kumar, D. Welti, R. R. Ernst, *J. Magn. Res.* **18**, 69 (1975); W. A. Edelstein, J. M. S. Hutchison, G. Johnson, T. Redpath, *Phys. Med. Biol.* **25**, 751 (1980).
12. A. N. Garroway, P. K. Grannell, P. Mansfield, *J. Phys. C* **7**, L457 (1974).
13. P. Mansfield and P. K. Grannell, *Phys. Rev. B* **12**, 3618 (1975); L. Feiner and P. R. Locher, *Appl. Phys.* **22**, 257 (1980); S. Ljunggren, *J. Magn. Reson.* **54**, 338 (1983); D. B. Twieg, *Med. Phys.* **10**, 610 (1983); K. F. King, *ibid.* **11**, 1 (1984).
14. E. L. Hahn, *Phys. Rev.* **80**, 580 (1950).
15. M. L. Winkler *et al.*, *Radiology* **166**, 17 (1988); R. B. Buxton *et al.*, *J. Comput. Assisted Tomogr.* **11**, 7 (1987).
16. R. Damadian, *Science* **171**, 1151 (1971); M. Komiyama *et al.*, *Am. J. Neuroradiol.* **8**, 65 (1987).
17. W. G. Bradley *et al.*, *Radiology* **156**, 93 (1985); W. Kucharczyk *et al.*, *ibid.* **161**, 761 (1986).
18. C. T. W. Moonen, P. C. M. van Zijl, J. A. Frank, D. Le Bihan, E. D. Becker, *Science* **250**, 53 (1990).
19. J. Frahm *et al.*, *Magn. Reson. Med.* **13**, 150 (1990); D. Chien *et al.*, *Magn. Reson. Imaging* **8**, 829 (1990).
20. G. Johnson and J. M. S. Hutchison, *J. Magn. Reson.* **63**, 14 (1985).
21. M. Doyle *et al.*, *Lancet* **ii**, 682 (1986).
22. B. Chapman *et al.*, *Magn. Reson. Med.* **5**, 246 (1987).
23. J. H. Kim *et al.*, paper presented at the Fifth Annual Meeting of the Society of Magnetic Resonance in Medicine, Montreal, 12 to 24 August 1986 (book of abstracts, p. 659); A. Macovski and C. Meyer, *ibid.*, p. 156; C. B. Ahn, J. H. Kim, Z. H. Cho, *IEEE Trans. Med. Imaging* **5**, 2 (1986); A. Macovski, *Magn. Reson. Med.* **2**, 29 (1985).
24. J. Hennig, A. Nauwerth, H. Friedburg, *Magn. Reson. Med.* **3**, 823 (1986).
25. M. K. Stehling, R. J. Ordidge, P. Mansfield, paper presented at the Eighth Annual Meeting of the Society of Magnetic Resonance Imaging, Washington, DC, 20 to 23 February 1990 (book of abstracts, p. 50).
26. M. K. Stehling *et al.*, *Magn. Reson. Med.* **13**, 514 (1990).
27. I. R. Young *et al.*, *J. Comput. Assisted Tomogr.* **6**, 1 (1982); F. W. Wehrli *et al.*, *ibid.* **8**, 369 (1984); I. R. Young, M. Burl, G. M. Bydder, *ibid.* **10**, 271 (1986); R. E. Hendrick, T. R. Nelson, W. R. Hendee, *Magn. Reson. Imaging* **2**, 193 (1984).
28. D. Chien, D. J. Atkinson, R. R. Edelman, *J. Magn. Reson. Imaging* **1**, 63 (1991).
29. R. J. Ordidge, P. Gibbs, B. Chapman, M. K. Stehling, P. Mansfield, *Magn. Reson. Med.* **16**, 238 (1990).
30. L. R. Ehman, *Am. J. Roentgenol.* **143**, 1175 (1985); D. R. Bailes, *J. Comput. Assisted Tomogr.* **9**, 835 (1985); E. M. Haacke and J. L. Patrick, *J. Magn. Reson. Imaging* **4**, 359 (1986); C. E. Lewis, *Radiology* **160**, 803 (1986); P. M. Pattany *et al.*, *J. Comput. Assisted Tomogr.* **11**, 369 (1987).
31. L. Kaufman *et al.*, *Circulation* **67**, 251 (1983); R. Dinsmore, in *Clinical Magnetic Resonance Imaging*, R. R. Edelman and J. R. Hesselink, Eds. (Saunders, Philadelphia, 1990), chap. 27.
32. E. Krestel, *Imaging Systems for Medical Diagnostics* (Siemens AG, Berlin, 1990).
33. H. L. Kantor *et al.*, paper presented at the Seventh Annual Meeting of the Society of Magnetic Resonance in Medicine, San Francisco, 20 to 26 August 1988 (book of abstracts, p. 246); N. Wilke *et al.*, *Radiology*, in press.
34. L. Axel, *Am. J. Roentgenol.* **143**, 1157 (1984); D. J. Bryant, J. A. Payne, D. N. Firmin, D. B. Longmore, *J. Comput. Assisted Tomogr.* **8**, 588 (1984); D. A. Feinberg, L. E. Crooks, P. Sheldon, *Magn. Reson. Med.* **2**, 555 (1985); R. J. Ordidge, D. N. Guilfoyle, P. Gibbs, P. Mansfield, paper presented at the Eighth Annual Meeting of the Society of Magnetic Resonance in Medicine, Amsterdam, 12 to 18 August 1989 (book of abstracts, p. 889); J. R. Singer, *Science* **130**, 1652 (1959).
35. M. K. Stehling *et al.*, paper presented at European Congress of NMR in Medicine and Biology, Berlin, 1988 (book of abstracts, p. 64); M. K. Stehling *et al.*, *Br. J. Radiol.* **64**, 89 (1991).
36. D. N. Firmin *et al.*, *Magn. Reson. Med.* **12**, 316 (1989).
37. M. K. Stehling *et al.*, paper presented at the European Congress of NMR in Medicine and Biology, Berlin, 1988 (book of abstracts, p. 258); M. K. Stehling *et al.*, *Am. J. Roentgenol.* in press.
38. W. G. Bradley, K. E. Kortman, B. Burgoyne, *Radiology* **159**, 611 (1986); D. A. Feinberg and A. S. Mark, *ibid.* **163**, 793 (1987); J. B. Rubin and D. R. Enzman, *Am. J. Roentgenol.* **148**, 973 (1987).
39. V. J. Wedeen *et al.*, paper presented at the Ninth Annual Meeting of the Society of Magnetic Resonance in Medicine, New York, 18 to 24 August 1990 (book of abstracts, p. 164); K. Kose, *ibid.*, p. 168.
40. *Cancer Facts and Figures* (American Cancer Society, New York, 1985); M. A. Adson, *Am. J. Roentgenol.* **140**, 695 (1983).
41. D. D. Stark *et al.*, *Am. J. Roentgenol.* **145**, 213 (1985); J. T. Ferrucci, *ibid.* **147**, 1103 (1986); S. Saini *et al.*, *ibid.*, p. 357.
42. M. K. Stehling *et al.*, paper presented at the 75th Annual Meeting of the Radiological Society of North America, Chicago, 1989 (book of abstracts, p. 337); M. K. Stehling, D. F. Evans, P. Mansfield, paper presented at the Eighth Annual Meeting of the Society of Magnetic Resonance Imaging, Washington, DC, 20 to 23 February 1990 (book of abstracts, p. 101); M. K. Stehling *et al.*, *Radiology*, in press.
43. M. K. Stehling *et al.*, *Br. J. Radiol.* **63**, 430 (1990).
44. M. K. Stehling *et al.*, *Radiology* **171**, 41 (1989).
45. R. R. Rzedzian, paper presented at the Sixth Annual Meeting of the Society of Magnetic Resonance in Medicine, New York, 1987 (book of abstracts, p. 229).
46. K. D. Merboldt *et al.*, *Magn. Reson. Med.* **9**, 423 (1989); D. A. Feinberg and A. S. Mark, *Radiology* **163**, 793 (1987).
47. D. Le Bihan *et al.*, *Radiology* **161**, 401 (1986); D. Le Bihan *et al.*, *ibid.* **168**, 497 (1988).
48. E. O. Stejskal and J. E. Tanner, *J. Chem. Phys.* **42**, 288 (1965).
49. T. L. Chenevert, J. A. Brunberg, J. G. Pipe, *Radiology* **177**, 401 (1990).
50. D. Le Bihan *et al.*, *J. Comput. Assisted Tomogr.* **15**, 19 (1991); C. T. W. Moonen *et al.*, *Radiology* **171**, 853 (1989).
51. R. Turner *et al.*, *Radiology* **177**, 407 (1990); H. E. Avram and L. E. Crooks, paper presented at the Seventh Annual Meeting of the Society of Magnetic Resonance in Medicine, San Francisco, 20 to 26 August 1988 (book of abstracts, p. 980).
52. M. E. Moseley, J. Kucharczyk, J. Mintorovitch, *Am. J. Neuroradiol.* **11**, 423 (1990).
53. M. E. Moseley *et al.*, *Radiology* **176**, 439 (1990).
54. D. Le Bihan, J. Delannoy, R. L. Levin, *ibid.* **171**, 853 (1989).
55. N. Higuchi *et al.*, paper presented at the Ninth Annual Meeting of the Society of Magnetic Resonance in Medicine, New York, 18 to 24 August 1990 (book of abstracts, p. 638).
56. J. Delannoy, D. Le Bihan, D. I. Hoult, R. L. Levin, *Med. Phys.* **17**, 855 (1990).
57. B. R. Rosen, J. W. Belliveau, J. M. Vevea, T. J. Brady, *Magn. Reson. Med.* **14**, 249 (1990); J. W. Belliveau *et al.*, paper presented at the Ninth Annual Meeting of the Society of Magnetic Resonance Imaging, Chicago, 13 to 17 April 1991 (book of abstracts, p. 202).
58. B. R. Rosen, J. W. Belliveau, D. Chien, *Magn. Reson. Q.* **5**, 263 (1989).
59. D. L. White, M. F. Wendland, K. P. Aicher, A. A. Tzika, M. E. Moseley, paper presented at the Ninth Annual Meeting of the Society of Magnetic Resonance in Medicine, New York, 18 to 24 August 1990 (book of abstracts, p. 57).
60. N. Patronas *et al.*, *Neuroradiology* **33** (suppl.), 267 (1991); M. K. Stehling *et al.*, paper presented at the Eighth Annual Meeting of the Society of Magnetic Resonance in Medicine, Amsterdam, 12 to 18 August 1989 (book of abstracts, p. 358).
61. M. K. Stehling *et al.*, *Lancet* **ii**, 157 (1989); M. K. Stehling *et al.*, *Magn. Reson. Med.* **13**, 314 (1990); P. Mansfield *et al.*, *Br. J. Radiol.* **63**, 833 (1990).
62. A. Chrispin *et al.*, *Paediatr. Radiol.* **16**, 293 (1986); C. O'Callaghan *et al.*, *Ann. Radiol.* **30**, 470 (1987).
63. H. Fischer, paper presented at the 75th Annual Meeting of the Radiological Society of North America, Chicago, 1989 (book of abstracts, p. 276); M. S. Cohen, R. M. Weisskoff, R. R. Rzedzian, H. L. Kantor, *Magn. Reson. Med.* **14**, 409 (1990).
64. J. P. Reilly, *Med. Biol. Eng. Comput.* **27**, 101 (1989).
65. P. Mansfield *et al.*, *Philos. Trans. R. Soc. London Ser. A* **333**, 495 (1990).
66. T. F. Budinger, H. Fischer, D. Hentschel, H-E. Reinfelder, F. Schmitt, paper presented at the Ninth Annual Meeting of the Society of Magnetic Resonance in Medicine, New York, 18 to 24 August 1990 (book of abstracts, p. 276); J. D. Bourland *et al.*, *ibid.*, p. 1157.
67. L. E. Crooks *et al.*, *Radiology* **166**, 157 (1988).
68. D. A. Feinberg, R. Turner, P. Jakob, M. von Kienlin, *Magn. Reson. Med.* **13**, 162 (1990).
69. R. Turner, *J. Phys. E* **21**, 948 (1988).
70. P. Mansfield and B. Chapman, *J. Magn. Reson.* **72**, 211 (1987); R. Turner and R. M. Bowley, *J. Phys. E* **19**, 876 (1986); P. B. Roemer, W. A. Edelstein, J. S. Hickey, paper presented at the Fifth Annual Meeting of the Society of Magnetic Resonance in Medicine, Montreal, 12 to 24 August 1986 (book of abstracts, p. 1067).
71. We acknowledge technical assistance from GE Medical Systems and Siemens AG, and the help of colleagues in the In Vivo NMR Center of the National Institutes of Health, and the University of Nottingham.